Research Square

Preprints are preliminary reports that have not undergone peer review.
They should not be considered conclusive, used to inform clinical practice,
or referenced by the media as validated information.

Understanding the Efficacy of Concentrated Interstitial Carbon in Enhancing the Pitting Corrosion Resistance of Stainless Steel

Tianshu Li
The Ohio State University
Szu-Chia Chien
The Ohio State University
Zhe Ren
Case Western Reserve University
Wolfgang Windl
Ohio State University https://orcid.org/0000-0001-5892-0684
Frank Ernst
Case Western Reserve University
Gerald Frankel (frankel.10@osu.edu)
The Ohio State University https://orcid.org/0000-0003-0573-3548

Article

Keywords: Low Temperature Carbuization, Austenitic Stainless Steel, Passive Film Properties, Metal Dissolution Rate, Corrosion Resistance Alloys

Posted Date: January 8th, 2021

DOI: https://doi.org/10.21203/rs.3.rs-135203/v1

License: This work is licensed under a Creative Commons Attribution 4.0 International License.
Read Full License

Version of Record: A version of this preprint was published at Acta Materialia on December 1st, 2021. See the published version at https://doi.org/10.1016/j.actamat.2021.117433.

Abstract

By introducing a high fraction of interstitial carbon through low temperature carburization, the pitting corrosion resistance of austenitic stainless steel can be significantly improved. Previous work attributed this enhancement to the improvement of passive film properties. However, we show here that interstitial carbon actually *weakens* the passive film on stainless steel. In fact, the enhancement in pitting resistance is a result of carbon *reducing the metal dissolution rate* in a local pit environment by many orders of magnitude, which extremely decreases the growth stability of a pit and prevents it from transitioning into stable growth. Electronic structure calculations show that carbon *bonds* to the metal atoms and that the metal–carbon bonds are 1.6 to 2.0 times stronger than the metal–metal bonds. Different from prior theories, we show that the significant increase of pitting resistance originates from the formation of covalent bonds between interstitial carbon and its neighboring metal atoms, resulting in a significantly reduced dissolution rate. This study indicates a new strategy for the design of corrosion resistant alloys, namely alloying with concentrated interstitials that form strong bonds with the matrix atoms.

Main Text

To meet the fast-growing demand of alloys serving in harsh environments, great efforts have been made to design alloys combining enhanced mechanical properties and improved corrosion resistance.[1, 2] One strategy to achieve this goal is to modify the alloy surface using surface engineering techniques, such as carburization. The deleterious precipitation of intergranular Cr carbides during carburization of stainless steels by standard methods can be prevented by *low temperature carburization* (LTC),[3, 4, 5] which allows the diffusion of carbon atoms into the alloy matrix resulting in a high concentration, without precipitation of carbides. Generally, carbon atoms are incorporated in the octahedral sites of face-centered cubic (FCC) structures, forming a subsurface zone of concentrated interstitial carbon, with carbon fraction up to 0.15 and the mean depth on the order of 10 mm.[6] Even low concentrations of interstitial carbon can improve the corrosion properties of iron,[7, 8] but the benefits are small relative to those imparted by higher concentrations.

Concentrated interstitial carbon was widely reported to improve the corrosion resistance of stainless steel,[3, 4, 5, 9, 10, 11, 12, 13, 14, 15, 16, 17, 18] Ni-based superalloys,[19] and high entropy alloys.[20] Most previous studies focused on the changes in passive film properties.[4, 10, 11, 12, 13, 16, 18, 20, 21] However, no consensus regarding the underlying mechanism has been reached. Some considered that the interstitial carbon increased passivity, including the growth kinetics and stability of the passive film,[4, 10, 12, 21] while some others espoused the totally opposite opinion.[13, 16] Furthermore, in some studies the passive current density of carburized samples, a key parameter to evaluate the passivity, was found to be lower than or similar to untreated samples,[3, 4, 10, 14] while others have reported higher passive current densities for carburized samples.[11, 15, 17] Clearly, the change in passive film properties is not a satisfactory explanation for the greatly improved corrosion resistance, and the effect of interstitial carbon needs to be further explored.

Generally, the evolution of a corrosion pit occurs in three stages: pit nucleation, metastable pit growth and stable pit growth. According to a recently proposed unified framework for pitting corrosion,[22, 23, 24, 25, 26] there are two critical steps that will influence the overall pitting process: (1) pit initiation associated with the breakdown of the passive film; (2) the transition from metastable pit to stable pit growth. The corrosion resistance of an alloy can be attributed to either the resistance to passive film breakdown, which is determined by the passive film properties, or the resistance to the transition of a pit from metastable to stable growth, or both.

To better understand the key role of concentrated interstitial carbon in enhancing the pitting corrosion resistance, its effect on pit stability must be understood. According to the unified pitting framework,[22, 23, 24, 25, 26] pit stability can be evaluated by the parameter $i_{diss,max}$, which is the pit dissolution current density in the salt-film-free state and is also the maximum dissolution current density that a pit can achieve under given conditions. A larger $i_{diss,max}$ corresponds to a greater ability to stabilize a pit, thus promoting the transition of a pit from metastable to stable pit growth. In contrast, a lower $i_{diss,max}$ represents a lower pit stability thus a higher pitting corrosion resistance. A detailed description of pit growth stability is described in Supplementary Materials. In this study, we demonstrate that the superior pitting resistance of carburized alloy is not derived from the changes in passive film properties, but should be attributed to the significantly reduced $i_{diss,max}$ because of the strong covalent bonds formed between interstitial carbon and its neighboring metal atoms, making it more energetically difficult to dissociate metal atoms for metal dissolution.

Origin of Superior Pitting Resistance: Passive Film Breakdown vs. Pit Growth Stability

To exclude effects of the untreated substrate, fully carburized AISI 316 stainless steel (hereafter referred to as SS316) foils (50 mm in thickness) and wires (51 mm in diameter) were prepared by LTC treatment. Details of the samples are given in the Supplementary Materials. **Figure 1a** shows typical cyclic potentiodynamic polarization (CPP) curves of carburized and untreated foil samples tested in 0.6 M NaCl at room temperature. Although the carburized SS316 sample exhibited a lower breakdown potential compared with the untreated sample and the carburized sample was polarized to high potentials, no severe corrosion attack was observed on the carburized sample after the tests (**Figure 1b**). The light corrosion attack likely originated from the transpassive dissolution at high potentials, rather than pitting corrosion, which is in agreement with the small positive hysteresis observed during the reverse scan. In contrast, the curve of the untreated sample exhibits a large positive hysteresis (**Figure 1b**), and large penetrating pits were observed after the test (**Figure 1c**). Therefore, in spite of a lower breakdown potential, the pitting resistance of the carburized sample is actually significantly higher than that of the untreated sample. On the other hand, the carburized SS316 also exhibits higher passive current density with substantial noise, probably associated with metastable pitting events. This indicates that the passive film formed on the carburized SS316 is less protective than that of the untreated SS316. Additionally, in the region between the breakdown and transpassive dissolution, the carburized SS316 exhibited pseudo passivity with the nominal current density of about 10^{-4} A cm^{-2}, which is about one

order of magnitude higher than the passive current density before breakdown. The breakdown associated with the increase in current density at the potential of about 0.28 V_{SCE} is really a transition from passivity to another condition, referred to here as pseudo passivity. Note that this pseudo passivity is not a true passive state for stainless steel as the current density is significantly higher than that in the passive regime. Furthermore, different than the untreated sample, the carburized SS316 did not fully repassivate during the reverse scan but again exhibited pseudo passivity, indicating that the repassivation ability of the carburized sample is much lower than that of the untreated sample. Based on the CPP results, it can be seen that the carburized SS316 forms a weak passive film, and its resistance to passive film breakdown and the ability to repassivate after the breakdown is actually low. Therefore, the superior pitting resistance of carburized SS316 is not derived from improvements in passive film properties.

To investigate the pit growth stability, untreated and fully carburized SS316 wires were made into one-dimensional (1D) artificial pit electrodes,[26] which are able to create a single pit, allowing pit growth in one direction (**Figure 2a**). **Figure 2b** shows CPP curves for 1D electrodes in 0.6 M NaCl solution at room temperature. The absence of metal at the pit mouth after the tests, as indicated by the black round area in the inserted optical images, shows that both samples experienced considerable dissolution and 1D pits were successfully created. The electrochemical behavior of the carburized SS316 1D electrode is similar to that of the carburized foil sample (**Figure 1a**), exhibiting passivity, a lower breakdown potential and a current peak, followed by pseudo passivity and transpassivity. The behavior after reversal of scanning is also the same: a small hysteresis followed by pseudo passivity. The decrease of current density to the pseudo passive level indicates that the 1D pit could not transition into stable growth even though it experienced high rate dissolution in the transpassive region. The untreated SS316 1D electrode exhibited different behavior than the untreated foil sample; breakdown was not observed until at high potentials associated with transpassive dissolution. After a period of reverse scan that followed back along the upward scan, the transpassive dissolution transitioned into stable 1D pit growth under diffusion control, as indicated by the increase in current density to a high stable value. The slight decrease of the current during the following downward scanning is typical of diffusion-controlled 1D pit growth caused by the effect of increasing pit depth on the diffusion-limited current density. Additionally, the 1D pit of untreated SS316 exhibited clear repassivation at low potentials associated with a sharp decrease in current. CPP measurements of 1D electrodes were also performed in 1 M HCl (**Figure 2c**). In such a harsh environment, the untreated SS316 is still able to passivate, as indicated by the clear active-passive transition followed by a broad passive region. Stable diffusion limited 1D pit growth was also observed in the reverse scan. In contrast, the carburized SS316 did not fully passivate and only exhibited pseudo passivity with current density on the order of 10^{-3} A cm^{-2}. However, even in this harsh bulk environment, the carburized SS316 1D pit still did not develop into to stable 1D pit growth, as indicated by the small hysteresis during the reverse scan. Based on CPP tests on 1D electrodes, it can be seen that, although the carburized SS316 exhibited a much lower resistance to passive film breakdown, its resistance to the transition of a pit to stable growth is extremely high.

To quantitatively evaluate the pit growth stability, the metal dissolution rate in local pit environment, i.e. $i_{diss,max}$, must be determined. According to the unified pitting framework,[26] $i_{diss,max}$ must be measured from a growing pit under charge transfer control, which corresponds to the salt-film-free condition. CPP tests show that the carburized SS316 exhibits pseudo passivity at potentials below the transpassive region (**Figure 2b**). Therefore, $i_{diss,max}$ of carburized samples can only be measured within the transpassive region where active dissolution is achieved. **Figure 2d** shows the potentiostatic polarization of a carburized SS316 1D electrode initiated at 1.2 V_{SCE}. The continuous increase of current density is generated by the increase of pit solution concentration at the pit surface, and it indicates that the 1D pit growth remains under charge transfer control.[26] Therefore, the measured pit current density is the $i_{diss,max}$ of carburized SS316 at 1.2 V_{SCE},[*] and it is on the order of 10^{-1} A cm^{-2}. After stepping to 0.7 V_{SCE}, the current density plunged to the pseudo passive level. In contrast, the untreated SS316 1D pit transitioned to diffusion-controlled pit growth immediately after the final breakdown, as indicated by the continuous decrease of the current density (**Figure 2e**). After stepping to 0.7 V_{SCE}, the diffusion-controlled pit growth was still maintained, which, again, indicates a much higher pit stability compared with the carburized sample. The diffusion-controlled pit growth indicates the presence of salt film on the pit surface, thus $i_{diss,max}$ of the untreated sample cannot be obtained directly from potentiostatic polarization measurements. The approach using a 1D electrode to determine $i_{diss,max}$ for alloys with relatively high pit stability has been developed previously.[26] The $i_{diss,max}$ of untreated SS316 at 1.2 V_{SCE} was determined and is on the order of 10^{10} A cm^{-2} (details described in Method), which is about 11 orders of magnitude higher than that of the carburized sample. According to the unified pitting framework,[22, 23, 24, 25, 26] the extremely reduced $i_{diss,max}$ will remarkably decrease the growth stability of a pit formed on carburized SS316, preventing it from transitioning into stable growth, thus significantly improving the pitting corrosion resistance of the carburized alloy.

Effect of Interstitial Carbon on Bond Strength of an Alloy System

According to a conceptual model developed by Marcus to explain the effects of certain alloying elements on localized corrosion,[27] the metal–metal bond strength is a fundamental property that will significantly influence the passivity and metal dissolution. Generally, the addition of dissolution moderators such as Mo, Nb, and W can increase the bond strength and make it energetically more difficult to separate metal atoms from the substrate. However, when a considerable amount of non-metallic elements is incorporated into the alloy without the formation of precipitates, the effect of non-metallic elements on the bond strength must be considered to interpret the behavior of passivity and metal dissolution (thus pit growth stability).

The effect of interstitial carbon on the bond strength of the FeCr:C alloy system can be evaluated by bond energies, which can be calculated using a recently developed bond-order bond energy (BOBE) model based on density-functional theory (DFT) calculations.[28] **Figure 3** shows the fitting of total bond energies ($E_{bond,tot}$) of a 32-metal-atom FeCr:C supercell (FCC structure) with various compositions. The extracted

metal–metal (M–M) and metal–carbon (M–C) bond energies are listed in Table 1 (detailed approach described in the Method section). A more negative bond energy value indicates a stronger bond. The calculated bond energies for Fe–C and Cr–C bonds are stronger than Fe–Fe and Cr–Cr bonds by a factor of 1.7 and 2.0, and stronger than Fe–Cr bonds by a factor of 1.8 and 1.6, respectively. Because the fitting is based on a variety of different FeCr:C compositions (28 in total), including those with and without interstitial carbon, the excellent fit quality suggests that the presence of interstitial carbon does not change the M–M bond strength in an appreciable way. Therefore, the formation of the added M–C bonds with significantly higher strength than the M–M bonds should be the crucial factor responsible for the decreased passivity and metal dissolution rate. Note that the bulk bond energies obtained here should be different from surface bond energies due to the different bonding situation. However, previous DFT work[29] has shown that the common approximation of direct proportionality between bulk and surface bonds[27, 30] is often justified. Our results thus suggest that if a metal atom on the surface is bonded to a neighboring interstitial carbon, it will have stronger bonding, making it more difficult for this atom to dissolve or break its bonds to participate in oxide formation.

To get further insight into the nature of the M–C bond, the charge density difference between the DFT-optimized ground state distribution in the solid and the superposition of the electron density of the unbound atoms was calculated for austenitic Fe with and without interstitial carbon. The redistribution of electrons in the solid allows for analysis of the types of bonds that form. Looking at pure Fe in **Figures 4a** and **b**, the electron distribution is found to be nearly uniform in the region between the metal ions, indicating that the valence electrons are more or less completely delocalized from their cores, which is consistent with the classical model of metallic bonding. **Figures 4c** and **d** show the charge density difference in the Fe_{32}:C_1 supercell. High electron accumulation can be found between the interstitial carbon and its neighboring Fe atoms, forming what is typically referred to as a bond charge in covalent solids.[31] These bond charges are typical of the bonding in group IV elemental semiconductors[32] and look equivalent to that of Fe–C bond obtained here.

Next, the density of states (DOS),[33] which is the number of electron states per unit volume at a given energy, was calculated to further investigate the nature of the Fe–C bonds. The local density of states (LDOS),[34] which is the density of states projected on the atomic orbitals of each atom, shows that, in the energy region from -7.5 to -5.0 eV and the region around -12.5 eV, new states (peaks) appear in the LDOS of the Fe atoms neighboring carbon, whose energy ranges overlap with peaks of the interstitial carbon LDOS (**Figure 5a**). Overlapping LDOS curves typically indicates the formation of a bond with hybridized orbitals found in covalent bonds and is expected for interstitial carbon in an octahedral site bonding to transition metal atoms, mainly involving σ bonds between the C 2s, 2p and Fe 4s orbitals, and π bonds between C 2p and Fe 3p, while the Fe 3d orbitals should be mostly non-bonding to carbon.[35, 36, 37] Screening should prevent such bonds from forming with Fe atoms outside of the carbon nearest-neighbor shell, which is indeed already the case for the second nearest Fe atom, where the LDOS has no peak and looks more or less identical to that in pure iron (**Figure 5a**). This is also in agreement with the charge density difference plot in **Figure 4d**, where the charge distribution around Fe atoms only differs from that

of pure Fe on the nearest Fe neighbors of the interstitial carbon. These findings are also in agreement with the calculated bond energy results and explain why interstitial carbon does not affect the M–M bond strength in the alloy.

Since the above qualitative comparisons suggest the formation of covalent bonding between Fe and interstitial carbon, pCOHP analysis was then performed to identify covalent bonding, nonbonding, and antibonding contributions for the electrons represented in the DOS. Positive values of -pCOHP indicate bonding states whereas negative values indicate anti-bonding states. **Figure 5b** shows the -pCOHP plot of an interstitial carbon atom and one of its neighboring Fe atoms. All bonding states are found below the Fermi level (E_F = 0 eV) and all antibonding states are found above the Fermi level, confirming covalent bonding characteristic between interstitial carbon and its neighboring Fe atoms.[38] **Figure 5c** compares the LDOS of interstitial carbon and Fe at the first neighbor site with the total -pCOHP and orbital-resolved -pCOHP results between interstitial carbon and neighboring Fe atoms. We found the dominating bonding states around −12.5 eV to involve C 2s and Fe 4s orbitals (**Figure 5c-iii**) as expected from molecular orbital theory,[36, 37] with a smaller contribution of C 2s – Fe 3d bonding (**Figure 5c-iv**), which is not observed in molecules.[36, 37] The bonding states in the energy range between −7 and −4 eV are contributed by σ bonding between the C 2p orbitals and Fe 4s orbitals (**Figure 5c-v**) as expected by molecular orbital theory, whose geometry/symmetry is mostly responsible for the octahedral bonding configuration, as well as weaker interactions between C 2p orbitals and Fe 3d and 3p orbitals (**Figures 5c-vi and 5c-vi;** the integral over the -pCOHP curve is a measure for the related bond strength). In addition, all the high LDOS values between −5 and 0 eV, which are from the Fe 3d orbitals, has -pCOHP values of zero and does not form covalent bonds. The Fe 3d orbitals are thus the main origin of the homogeneous charge density responsible for metallic bonding, as shown in **Figure 4**.

In addition to the covalent bond charges, the entire region of the interstitial carbon shows an increased charge density, accumulated from its Fe neighbors, which is similar to the situation in polar binary semiconductors such as SiC.[39] Such charge transfer is expected when considering the different electronegativities of Fe (1.83) and carbon (2.55), for which Pauling's theory[40] predicts 12% ionic character. To quantify the transfer, Bader charge analysis[41] was performed on the interstitial carbon and its six neighboring Fe atoms. The Bader charge of the interstitial carbon is -1.1, while that of neighboring Fe atoms is 0.12 with the discrepancy spilling to second-nearest neighbors with charge values around 0.03. Therefore, Fe–C bonds are of polar covalent nature, where the shared electrons in the bond charge are closer to the interstitial carbon atom. Such covalent bonds are also expected formed between interstitial carbon and other transition metal atoms, such as Cr (electronegativity 1.66), Ni (electronegativity 1.91), etc.

The formation of a covalent M–C bond is also supported by the Hall effect measurements on carburized SS316 foils, where the conduction electron concentration (N_e) was found to decrease with increasing concentration of interstitial carbon.[42] In light of the present findings, the decreased N_e of carburized SS316 should be attributed to the formation of covalent M–C bonds, where a portion of the mobile Fe

electrons become localized in the covalent M–C bonds. For the fully carburized foil with an average atomic fraction of 0.1 interstitial carbon, the N_e drops by 29%,[42] which approximates to the value of 33% obtained by theoretical analysis on covalent bonds. Detailed analysis is presented in the Supplementary Materials. As a result, both the electrical and thermal conductivities are decreased in the carburized alloy.[42] Additionally, XPS results on the carburized alloys, including both martensitic and austenitic steels,[8, 43] show that the electron binding energy of Fe atoms for the sample with high interstitial carbon is higher than that of the sample without interstitial carbon, which can also be attributed to the formation of covalent M–C bonds.

Summarizing the above analysis, there is strong and widespread evidence that interstitial carbon forms covalent bonds with its nearest neighbor metal atoms. It is also found that the effect of interstitial carbon is rather local and already becomes negligible for second nearest neighbors. If the added strong bonds are the dominant cause for increased pitting resistance and decreased passive film formation, this suggests that the concentration of interstitial carbon needs to be high for a significant effect, since only then the cumulative bond strength of the alloy system will be greatly increased. In that case, the covalent bonds formed by interstitial carbon can make it more energetically difficult to dissociate metal atoms for oxide formation or metal dissolution. The formation of M–C covalent bonds can thus well explain the low passivity and extremely low $i_{diss,max}$ (thus low pit growth stability) of carburized SS316 observed in this work. The fundamental understanding accomplished in this work provides a new strategy for designing highly corrosion resistant alloys, namely alloying concentrated interstitial atoms that form strong covalent/ionic bonds with the matrix atoms. Suitable alloying elements include but not limited to carbon; concentrated nitrogen and boron interstitials are also expected to have similar effects.

[*] Potential drop of the solution for carburized SS316 1D pit is calculated to be very small, only 0.034 V, thus it can be ignored. Therefore, the applied potential (1.2 V_{SCE}) can be considered as the potential at pit surface.

Methods

Materials

The commercial SS316 foils (McMASTER-Carr, Aurora, OH) and wires (California Fine Wire Company, Grover Beach, CA) used in this work meet the chemical composition requirements specified in ASTM A240 and ASTM A580, respectively. The foil thickness (50 mm) and wire diameter (51 mm) were selected based on the typical thickness of the case layer on LTC-treated SS316,[44] which allows the treated foil and wire to be nearly fully carburized throughout. LTC treatment of both the SS316 wire and foil specimens was performed using the gas phase process established by Swagelok.[45, 46, 47] Prior to the LTC treatment, the samples were ultrasonically cleaned in ethanol to remove grease and contaminants, and rinsed in deionized water. The specimens were then transferred into a gas furnace and processed with the following steps: (1) 10.8 ks of surface activation in a 0.10 MPa HCl and N_2 atmosphere (X_{HCl} = 0.9,

X_{N2} = 0.1) at 523 K; (2) 10.8 ks of carburization in a 0.10 MPa CO, H_2, and N_2 atmosphere (X_{CO} = 0.46, X_{H2} = 0.46, X_{N2} = 0.08) at 723 K; (3) Repeat of surface activation treatment in step 1; (4) Carburization for 72 ks at the same conditions used in step 2; (5) Cooling the samples down to room temperature. After LTC treatment, the samples were ultrasonically cleaned in deionized water to remove soot from the surface. No carbides were found in LTC treated samples (**Supplementary Figure 2**) and carbon distributed uniformly across the wire sample (**Supplementary Figure 3**).

Electrochemical Measurements

To evaluate the overall pitting corrosion resistance for both untreated and carburized SS316, electrochemical tests were first performed on the foil samples. The foils were connected to a Cu wire, wrapped with polytetrafluoroethylene tape and masked with silicone rubber, leaving an exposed working area around 40 mm^2 in size. The electrochemical tests were performed using a jacketed three-electrode cell connected to a programmable temperature-controlled circulator. The samples served as the working electrode, and a saturated calomel electrode (SCE) and Pt sheet were used as the reference and counter electrodes, respectively. To prepare the 1D artificial pit electrode, the SS316 wire was cast in epoxy with one end exposed and the other end connected to a Cu wire. The exposed electrode surface was ground to 1200 grit with SiC abrasive paper, ultrasonically cleaned in deionized water for 900 s, and dried with compressed air. For the electrochemical tests, the 1D electrode was placed upright in a vertical cell, a schematic of which was shown previously.[26] The testing solutions were prepared from deionized water and analytical grade chemicals, and a volume of 300 mL was used for each experiment. The electrochemical measurements in this work were carried out with a Gamry Reference 600 potentiostat.

Cyclic potentiodynamic polarization (CPP) tests were performed on untreated and carburized SS316 foil samples in aerated 0.6 M NaCl at room temperature. The samples were first potentiostatically polarized at -1.2 V_{SCE} for 10 min in an attempt to reduce the effect of air-formed oxide on the electrochemical behavior, and then kept in solution for 10 min to attain a stable open circuit potential (OCP). The CPP measurement was conducted at a scan rate of 1 mV s^{-1} in the upward direction starting at potential of -0.25 V versus OCP and was reversed at the anodic current of 1 mA. The test was terminated when repassivation or a cathodic current was achieved. The corrosion morphology was characterized using optical microscopy.

CPP tests were also performed on untreated and carburized SS316 1D artificial pit electrodes in both 0.6 M NaCl and 1 M HCl solutions at room temperature. Freshly ground 1D artificial pit electrodes were first stabilized in the test solutions for 10 min to attain a stable OCP. The CPP measurements were conducted at a scan rate of 1 mV s^{-1} in both upward and reverse directions. Potentiostatic polarization was also performed on 1D electrodes to explore the pit growth stability on both samples. An initial potential in the transpassive dissolution region, 1.2 V_{SCE}, was applied for a certain period to activate the electrode surface and grow the depth of the 1D pit, and the potential was then stepped down to 0.7 V_{SCE}.

The current was recorded at an acquisition frequency of 1 Hz. The corrosion morphology of the 1D pit was examined with optical microscopy.

Determination of Pit Dissolution Kinetics for Untreated SS316

$i_{diss,max}$ is the dissolution current density for the salt-film-free state of a pit, and its dependence on potential represents the pit dissolution kinetics. In contrast to carburized SS316, $i_{diss,max}$ of untreated SS316 cannot be measured using potentiostatic polarization because the pit growth will immediately transition to diffusion control, accompanied with salt film precipitation after the pitting breakdown occurs. To measure $i_{diss,max}$ for such alloys, a 1D pit must be scanned downward from the diffusion-controlled potential region into the charge-transfer-controlled region. $i_{diss,max}$ in saturated pit solution can be determined at the transition point from diffusion to charge transfer control. Such a test must be repeated at different pit depths to obtain $i_{diss,max}$ at different potentials. Details of the measurement on SS316 1D artificial pit electrodes have been reported previously and $i_{diss,max}$ for SS316 in saturated pit solution was obtained to be[26]

$$i_{diss,max} = A\ 10^{\frac{E_{max}}{b_a}}, \qquad (1)$$

where E_{max} is the potential (V_{SCE}) applied at the pit surface in the salt-film-free state; A is a constant, 1.964 A cm^{-2}; b_a is the anodic Tafel slope of metal dissolution in saturated pit solution, 0.116 V dec^{-1}. According to the above equation, the $i_{diss,max}$ of untreated SS316 at 1.2 V_{SCE} is determined to be on the order of 10^{10} A cm^{-2}. This value is significantly larger than the diffusion limited current density, so it is never achieved. However, it reflects the current density expected at a pit surface potential of 1.2 V_{SCE} in the absence of a salt film.

DFT Calculations of Metal–Metal and Metal–Carbon Bond Energies

Both passive film formation and metal dissolution require breaking of metal atom bonds at the alloy surface. To study the effect of interstitial carbon on bond strength, the bond energies of metal–metal (M–M) and metal–carbon (M–C) were calculated using a recently developed bond-order bond energy (BOBE) model.[28] The BOBE model parameterizes DFT-calculated energies of alloys, which are calculated for a range of alloy compositions, into pairwise bond energies in the spirit of the quasichemical solution model (QSM). In addition, the BOBE model considers that, for a binary alloy (AB), A- and B-rich ends can have different bonding strengths or even form different phases, such as FCC and BCC, which is different from the assumption made in QSM model. To accommodate this, a bond order function is introduced to model the transition between competing phases and switching their respective bond energies on and off. Previous work showed that the BOBE model can be used to describe the phase diagrams in the Ni–Cr–

Mo system, and the prediction is in excellent agreement with experimental phase diagrams.[28] In addition, enthalpies of mixing calculated from the bond energies agree with the DFT calculated results within just a few hundredths of an eV difference.

In this work, the bond energies of Fe–Fe, Cr–Cr, Fe–Cr, Fe–C, and Cr–C in FeCr:C alloys were calculated for Fe-rich alloys under the initial assumption that Cr and interstitial carbon concentrations are low enough that no switching function needed to be employed, which means staying within the classic QSM model. The excellent quality of the fit in **Figure 3** shows that this assumption was valid and a switching function was not needed. The M–M and M–C bond energies were calculated using the following steps: (i) Determine the total energies of *N*-metal-atom supercells with FCC structure for different compositions $Fe_{N-m}Cr_mC_l$ by DFT calculations, denoted as $E_{tot}(Fe_{N-m}Cr_mC_l)$, where N is the total atom number of metal atoms in the supercell, while m and l are the atom numbers of substitutional Cr and interstitial carbon atoms, respectively; (ii) Obtain the total bond energies ($E_{bond,tot}$) by subtracting the atomic energies from $E_{tot}(Fe_{N-m}Cr_mC_l)$:

$$E_{bond,tot}(m,l) = E_{tot}(Fe_{N-m}Cr_mC_l) - (N - m)E_{Fe} - mE_{Cr} - lE_C, \quad (2)$$

where E_{Fe}, E_{Cr} and E_C are the free atomic energy for Fe, Cr and C, respectively; (ii) Count the number of each bond in each cell, where n_{Fe-Fe}, n_{Cr-Cr}, n_{Fe-Cr}, n_{Fe-C} and n_{Cr-C} represent the number of Fe–Fe, Cr–Cr, Fe–Cr, Fe–C, and Cr–C bonds, respectively; (iv) Fit the respective bond energies to the total bond energies for the entire set of alloys:

$$E_{bond,tot}(m,l) = n_{Fe-Fe}\,\varepsilon_{Fe-Fe} + n_{Cr-Cr}\,\varepsilon_{Cr-Cr} + n_{Fe-Cr}\,\varepsilon_{Fe-Cr} + n_{Fe-C}\,\varepsilon_{Fe-C} + n_{Cr-C}\,\varepsilon_{Cr-C}, \quad (3)$$

where ε_{Fe-Fe}, ε_{Cr-Cr}, ε_{Fe-Cr}, ε_{Fe-C}, ε_{Cr-C} are the bond energies for Fe–Fe, Cr–Cr, Fe–Cr, Fe–C, and Cr–C, respectively.

The total energies of different supercells, $E_{tot}(Fe_{N-m}Cr_mC_l)$, were calculated using the Vienna *Ab-initio* Simulation Package (VASP)[48, 49] with projector augmented wave Perdew-Burke-Ernzerhof (PAW-PBE) potentials.[50] An energy cut-off of 400 eV was employed, and all supercells were fully relaxed with respect to atomic positions and lattice parameters while keeping a cubic crystal structure. Special quasirandom structures (SQS)[51, 52] with 32-metal-atom supercell (FCC structure) were used for the distribution of the metal atoms with 0, 2, 4, and 6 Cr atoms (0 to 18.75 at.%). In addition, 0, 1, 2, 3, and 4 interstitial carbon atoms (0 to 12.5 at.%) were included in the octahedral sites (**Supplementary Figure 4**). A 6×6×6 Monkhorst-Pack[53] k-point mesh was used for Brillouin-zone integration. All calculations were performed within collinear magnetism. An important question here concerns the magnetic state used in the DFT calculations. Neutron scattering showed that FCC iron has a spin density wave with axis along one of the cubic lattice vectors below its Néel temperature of 50 K[54], while it is paramagnetic at higher temperatures. Both magnetic states are impractical or impossible within the supercell calculations in this work. Jiang et al. examined the most sensible and practical magnetic state for DFT calculations and found that the

ferromagnetic high-spin phase with magnetic moments around 2.5 μ_B is the best approximation to predict the properties of paramagnetic iron,[55] which we adopted in this work.

To study the bonding formed between the interstitial carbon and the neighboring Fe atoms, charge density differences between electron distributions from full self-consistent DFT calculations and from a superposition of charge densities of the isolated atoms were calculated, which shows how the electrons rearrange when bonds are formed.[56] Additionally, the local electronic density of states was also simulated. Finally, the nature of the bonds was determined by projected crystal orbital Hamilton population (pCOHP) analysis, partitioning the band structure energy into different bonding states using the LOBSTER package[57, 58, 59, 60].

Declarations

Acknowledgements

This work was supported as part of the Center for Performance and Design of Nuclear Waste Forms and Containers, an Energy Frontier Research Center funded by the U.S. Department of Energy, Office of Science, Basic Energy Sciences under Award # DE-SC0016584. W.W.'s contributions were supported by AFOSR under Project # FA9550-19-1-0378. Dr. Joshua Goldberger is thanked for helpful discussions about interatomic bonding.

Author Contributions

T.L., W.W., F.E., and G.S.F. designed the research; T.L., S.C., and Z.R. performed the research; T.L., S.C., Z.R., and W.W. analyzed the data. All authors contributed to the editing of the paper, and approval of the content in its current form.

Data Availability

The data that support the findings of this study are available from the corresponding authors on reasonable request.

Competing Interest Statement

The authors declare that they have no known competing financial interests or personal relationships that could have appeared to influence the work reported in this paper.

References

1. Bell T. Current status of supersaturated surface engineered S-phase materials. Key Engineering Materials; 2008: Trans Tech Publ; 2008. p. 289-295.

2. Dong H. S-phase surface engineering of Fe-Cr, Co-Cr and Ni-Cr alloys. *International Materials Reviews* 2010, **55**(2)**:** 65-98.

3. Sun Y, Li X, Bell T. Low temperature plasma carburising of austenitic stainless steels for improved wear and corrosion resistance. *Surface Engineering* 1999, **15**(1)**:** 49-54.

4. Martin FJ, Natishan PM, Lemieux EJ, Newbauer TM, Rayne RJ, Bayles RA*, et al.* Enhanced Corrosion Resistance of Stainless Steel Carburized at Low Temperature. *Metallurgical and Materials Transactions A* 2009, **40**(8)**:** 1805-1810.

5. Natishan PM, Bayles RA, Rayne R, Longazel T, Martin FJ, Kahn H*, et al.* Interstitial Hardening of Type 316L Stainless Steel to Improve Corrosion Resistance and Mechanical Properties. *CORROSION* 2012, **68**(7)**:** 638-644.

6. Sun Y. Kinetics of low temperature plasma carburizing of austenitic stainless steels. *Journal of Materials Processing Technology* 2005, **168**(2)**:** 189-194.

7. Kadowaki M, Muto I, Sugawara Y, Doi T, Kawano K, Hara N. Pitting Corrosion Resistance of Martensite of AISI 1045 Steel and the Beneficial Role of Interstitial Carbon. *Journal of The Electrochemical Society* 2017, **164**(14)**:** C962-C972.

8. Kadowaki M, Saengdeejing A, Muto I, Chen Y, Masuda H, Katayama H*, et al.* First-principles analysis of the inhibitive effect of interstitial carbon on an active dissolution of martensitic steel. *Corrosion Science* 2020, **163:** 108251.

9. Sun Y. Response of cast austenitic stainless steel to low temperature plasma carburizing. *Materials & Design* 2009, **30**(4)**:** 1377-1380.

10. Sun Y. Corrosion behaviour of low temperature plasma carburised 316L stainless steel in chloride containing solutions. *Corrosion Science* 2010, **52**(8)**:** 2661-2670.

11. Martin FJ, Lemieux EJ, Newbauer TM, Bayles RA, Natishan PM, Kahn H*, et al.* Carburization-Induced Passivity of 316 L Austenitic Stainless Steel. *Electrochemical and Solid-State Letters* 2007, **10**(12)**:** C76.

12. Ha HY, Lee TH, Oh CS, Kim SJ. Effects of Carbon on the Corrosion Behaviour in Fe-18Cr-10Mn-N-C Stainless Steels. *steel research international* 2009, **80**(7)**:** 488-492.

13. Heuer AH, Kahn H, Ernst F, Michal GM, Hovis DB, Rayne RJ*, et al.* Enhanced corrosion resistance of interstitially hardened stainless steel: Implications of a critical passive layer thickness for breakdown. *Acta Materialia* 2012, **60**(2)**:** 716-725.

14. Kahn H, Heuer AH, Michal GM, Ernst F, Sharghi-Moshtaghin R, Ge Y*, et al.* Interstitial hardening of duplex 2205 stainless steel by low temperature carburisation: enhanced mechanical and electrochemical performance. *Surface Engineering* 2012, **28**(3)**:** 213-219.

15. Chiba A, Shibukawa S, Muto I, Doi T, Kawano K, Sugawara Y*, et al.* Microelectrochemical Aspects of Interstitial Carbon in Type 304 Stainless Steel: Improving Pitting Resistance at MnS Inclusion. *Journal of The Electrochemical Society* 2015, **162**(6)**:** C270-C278.

16. Niu W, Lillard RS, Li Z, Ernst F. Properties of the Passive Film Formed on Interstitially Hardened AISI 316L Stainless Steel. *Electrochimica Acta* 2015, **176:** 410-419.

17. Sugawara Y, Inoue W, Muto I, Hara N. A Methodology for Fabrication of Highly Pitting Corrosion-Resistant Type 304 Stainless Steel by Plasma Carburizing and Post-Pickling Treatment. *Journal of The Electrochemical Society* 2018, **165**(9)**:** C441-C449.

18. Rosalbino F, Scavino G, Ubertalli G. Passivity and its breakdown on low temperature plasma carburized AISI 204Cu stainless steel in chloride-containing solution. *Materials and Corrosion* 2018, **69**(5)**:** 563-571.

19. Sharghi-Moshtaghin R, Kahn H, Ge Y, Gu X, Martin FJ, Natishan PM*, et al.* Low-Temperature Carburization of the Ni-base Superalloy IN718: Improvements in Surface Hardness and Crevice Corrosion Resistance. *Metallurgical and Materials Transactions A* 2010, **41**(8)**:** 2022-2032.

20. Luo H, Zou S, Chen Y-H, Li Z, Du C, Li X. Influence of carbon on the corrosion behaviour of interstitial equiatomic CoCrFeMnNi high-entropy alloys in a chlorinated concrete solution. *Corrosion Science* 2020, **163:** 108287.

21. Sun Y. Depth-profiling electrochemical measurements of low temperature plasma carburised 316L stainless steel in 1M H2SO4 solution. *Surface and Coatings Technology* 2010, **204**(16)**:** 2789-2796.

22. Frankel GS, Li T, Scully JR. Localized Corrosion: Passive Film Breakdown vs Pit Growth Stability. *Journal of the Electrochemical Society* 2017, **164**(4)**:** C180-C181.

23. Li T, Scully JR, Frankel GS. Localized Corrosion: Passive Film Breakdown vs Pit Growth Stability: Part II. A Model for Critical Pitting Temperature. *Journal of The Electrochemical Society* 2018, **165**(9)**:** C484-C491.

24. Li T, Scully JR, Frankel GS. Localized Corrosion: Passive Film Breakdown vs. Pit Growth Stability: Part III. A Unifying Set of Principal Parameters and Criteria for Pit Stabilization and Salt Film Formation. *Journal of The Electrochemical Society* 2018, **165**(11)**:** C762-C770.

25. Li T, Scully JR, Frankel GS. Localized Corrosion: Passive Film Breakdown vs. Pit Growth Stability: Part IV. The Role of Salt Film in Pit Growth: A Mathematical Framework. *Journal of The Electrochemical Society* 2019, **166**(6)**:** C115-C124.

26. Li T, Scully JR, Frankel GS. Localized Corrosion: Passive Film Breakdown vs Pit Growth Stability: Part V. Validation of a New Framework for Pit Growth Stability Using One-Dimensional Artificial Pit Electrodes. *Journal of The Electrochemical Society* 2019, **166**(11)**:** C3341-C3354.

27. Marcus P. On some fundamental factors in the effect of alloying elements on passivation of alloys. *Corrosion Science* 1994, **36**(12)**:** 2155-2158.

28. Oberdorfer C, Windl W. Bond-order bond energy model for alloys. *Acta Materialia* 2019, **179:** 406-413.

29. Chien S-C, Windl W. Bond Synergy Model for Bond Energies in Alloy Oxides. *Journal of The Electrochemical Society* 2020, **167**(14)**:** 141511.

30. Taylor CD, Lu P, Saal J, Frankel GS, Scully JR. Integrated computational materials engineering of corrosion resistant alloys. *npj Materials Degradation* 2018, **2**(1)**:** 6.

31. Phillips JC. Covalent Bond in Crystals. I. Elements of a Structural Theory. *Physical Review* 1968, **166**(3)**:** 832-838.

32. Weber W. Adiabatic bond charge model for the phonons in diamond, Si, Ge, and alpha-Sn. *Physical Review B* 1977, **15**(10)**:** 4789-4803.

33. Pettifor DG, Cottrell AH. *Electron theory in alloy design*. The Institute of Materials Minerals and Mining, 1992.

34. Sholl D, Steckel JA. *Density functional theory: a practical introduction*. John Wiley & Sons, 2011.

35. Gray HB. Molecular orbital theory for transition metal complexes. *Journal of Chemical Education* 1964, **41**(1)**:** 2.

36. Scherbaum F, Grohmann A, Huber B, Krüger C, Schmidbaur H. Aurophilicity as a consequence of relativistic effects. *Angew Chem Int Ed Engl* 1988, **27:** 1544-1546.

37. Haberlen OD, Schmidbaur H, Roesch N. Stability of main-group element-centered gold cluster cations. *Journal of the American Chemical Society* 1994, **116**(18)**:** 8241-8248.

38. Nguyen TQ, Sato K, Shibutani Y. First-Principles Study of BCC/FCC Phase Transition Promoted by Interstitial Carbon in Iron. *Materials Transactions* 2018, **59**(6)**:** 870-875.

39. Karch K, Pavone P, Windl W, Schütt O, Strauch D. Ab initio calculation of structural and lattice-dynamical properties of silicon carbide. *Physical Review B* 1994, **50**(23)**:** 17054-17063.

40. Pauling L. *The Nature of the Chemical Bond*, vol. 260. Cornell university press Ithaca, NY, 1960.

41. Bader RF. *Atoms in Molecules: A Quantum Theory*. Clarendon Press, 1990.

42. Ren Z, Ernst F. Electronic impact of concentrated interstitial carbon on physical properties of AISI-316 austenitic stainless steel. *Acta Materialia* 2019, **173:** 96-105.

43. Chiba A, Koyama M, Akiyama E, Nishimura T. Interstitial Carbon Enhanced Corrosion Resistance of Fe-33Mn-xC Austenitic Steels: Inhibition of Anodic Dissolution. *Journal of The Electrochemical Society* 2018, **165**(2)**:** C19-C26.

44. Collins SR, Williams PC, Marx SV, Heuer A, Ernst F, Kahn H. Low-Temperature Carburization of Austenitic Stainless Steels. In: Dossett JL, Totten GE (eds). *Heat Treating of Irons and Steels*, vol. 4D. ASM International, 2014, p 0.

45. Williams PC, Collins SR. Mechanical design using low-temperature carburization. *JOM* 2008, **60**(12)**:** 27-30.

46. Ren Z, Heuer AH, Ernst F. Ultrahigh-strength AISI-316 austenitic stainless steel foils through concentrated interstitial carbon. *Acta Materialia* 2019, **167:** 231-240.

47. Ren Z, Ernst F. High-temperature phase transformations in AISI 316 stainless steel infused with concentrated interstitial carbon. *Journal of Alloys and Compounds* 2020, **819:** 153000.

48. Kresse G, Hafner J. Ab initio molecular dynamics for liquid metals. *Physical Review B* 1993, **47**(1)**:** 558-561.

49. Kresse G, Hafner J. Ab initio molecular-dynamics simulation of the liquid-metal–amorphous-semiconductor transition in germanium. *Physical Review B* 1994, **49**(20)**:** 14251-14269.

50. Kresse G, Joubert D. From ultrasoft pseudopotentials to the projector augmented-wave method. *Physical Review B* 1999, **59**(3)**:** 1758-1775.

51. Zunger A, Wei SH, Ferreira LG, Bernard JE. Special quasirandom structures. *Physical Review Letters* 1990, **65**(3)**:** 353-356.

52. van de Walle A, Tiwary P, de Jong M, Olmsted DL, Asta M, Dick A*, et al.* Efficient stochastic generation of special quasirandom structures. *Calphad* 2013, **42:** 13-18.

53. Monkhorst HJ, Pack JD. Special points for Brillouin-zone integrations. *Physical Review B* 1976, **13**(12)**:** 5188-5192.

54. Tsunoda Y. Spin-density wave in cubic γ-Fe and γ-Fe100-xCoxprecipitates in Cu. *Journal of Physics: Condensed Matter* 1989, **1**(51)**:** 10427-10438.

55. Jiang DE, Carter EA. Carbon dissolution and diffusion in ferrite and austenite from first principles. *Physical Review B* 2003, **67**(21)**:** 214103.

56. Levine RD. *Molecular reaction dynamics*. Cambridge University Press, 2009.

57. Dronskowski R, Blöchl PE. Crystal orbital Hamilton populations (COHP): energy-resolved visualization of chemical bonding in solids based on density-functional calculations. *The Journal of Physical Chemistry* 1993, **97**(33)**:** 8617-8624.

58. Deringer VL, Tchougréeff AL, Dronskowski R. Crystal Orbital Hamilton Population (COHP) Analysis As Projected from Plane-Wave Basis Sets. *The Journal of Physical Chemistry A* 2011, **115**(21)**:** 5461-5466.

59. Maintz S, Deringer VL, Tchougréeff AL, Dronskowski R. Analytic projection from plane-wave and PAW wavefunctions and application to chemical-bonding analysis in solids. *Journal of Computational Chemistry* 2013, **34**(29)**:** 2557-2567.

60. Maintz S, Deringer VL, Tchougréeff AL, Dronskowski R. LOBSTER: A tool to extract chemical bonding from plane-wave based DFT. *Journal of Computational Chemistry* 2016, **37**(11)**:** 1030-1035.

Table

Table 1. Pairwise bond energies in the bulk of FeCr:C alloy calculated with concentration of Cr up to 18.75 at.% and interstitial carbon up to 12.5 at.%.

Bonds	Fe–Fe	Fe–Cr	Cr–Cr	Fe–C	Cr–C
Bond Energy (eV)	-0.78	-0.73	-0.58	-1.31	-1.14

Figures

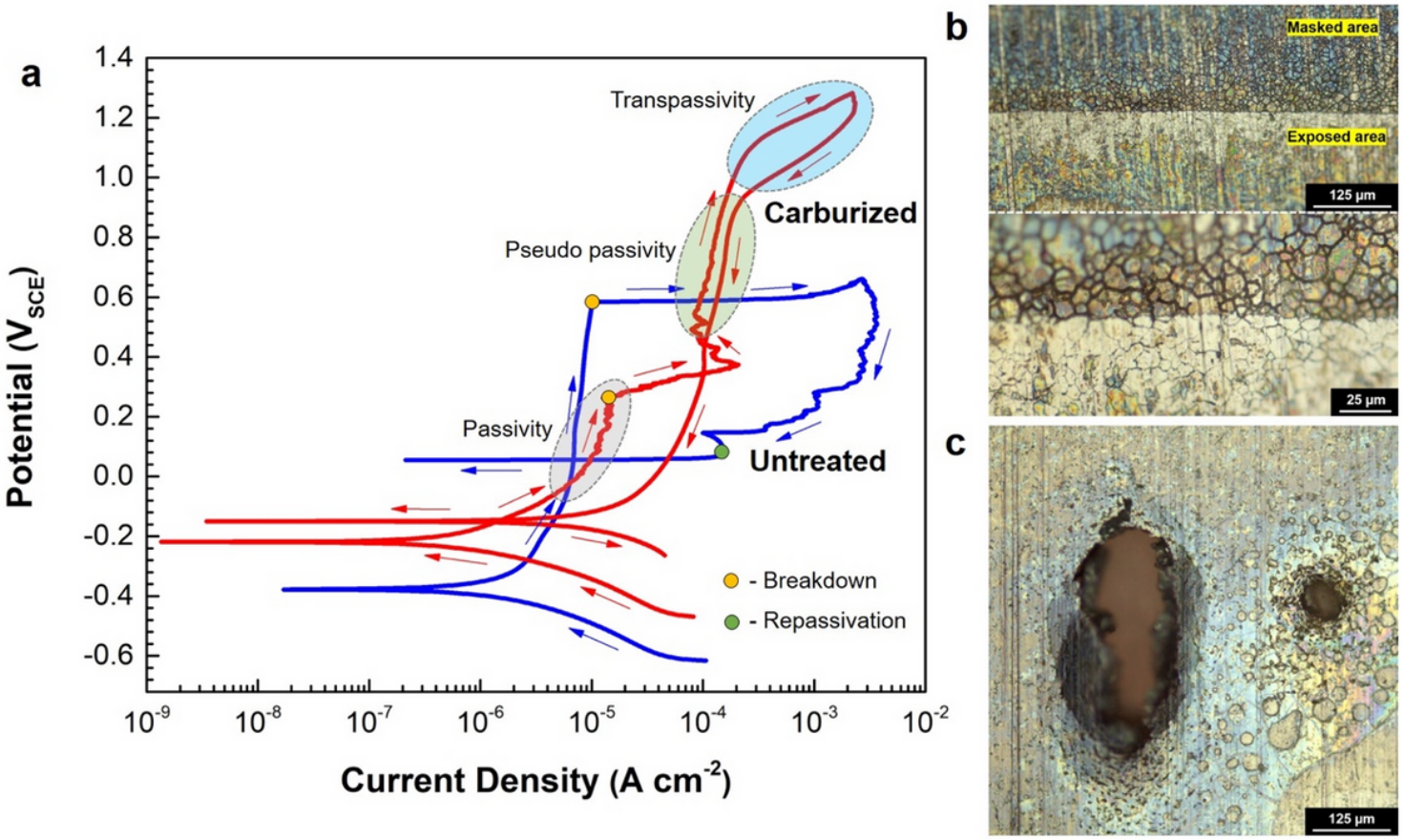

Figure 1

(a) Cyclic potentiodynamic polarization curves of untreated and carburized SS316 foils in 0.6 M NaCl solution at room temperature. (b) Light-optical microscopy image of carburized SS316 foil after the test. The exposed working area exhibited no evidence of corrosion. The masking materials were removed. The masked area underwent some slight local attack at the grain boundaries, generating shallow trenches with black deposit of released carbon, as seen in the magnified image. Although the potential was

scanned to high values in the transpassive dissolution region, the local attack did not penetrate deep into the substrate. (c) Light-optical corrosion morphology of untreated SS316 foil after the test. Two penetrating pits with typical lacy pit covers were observed.

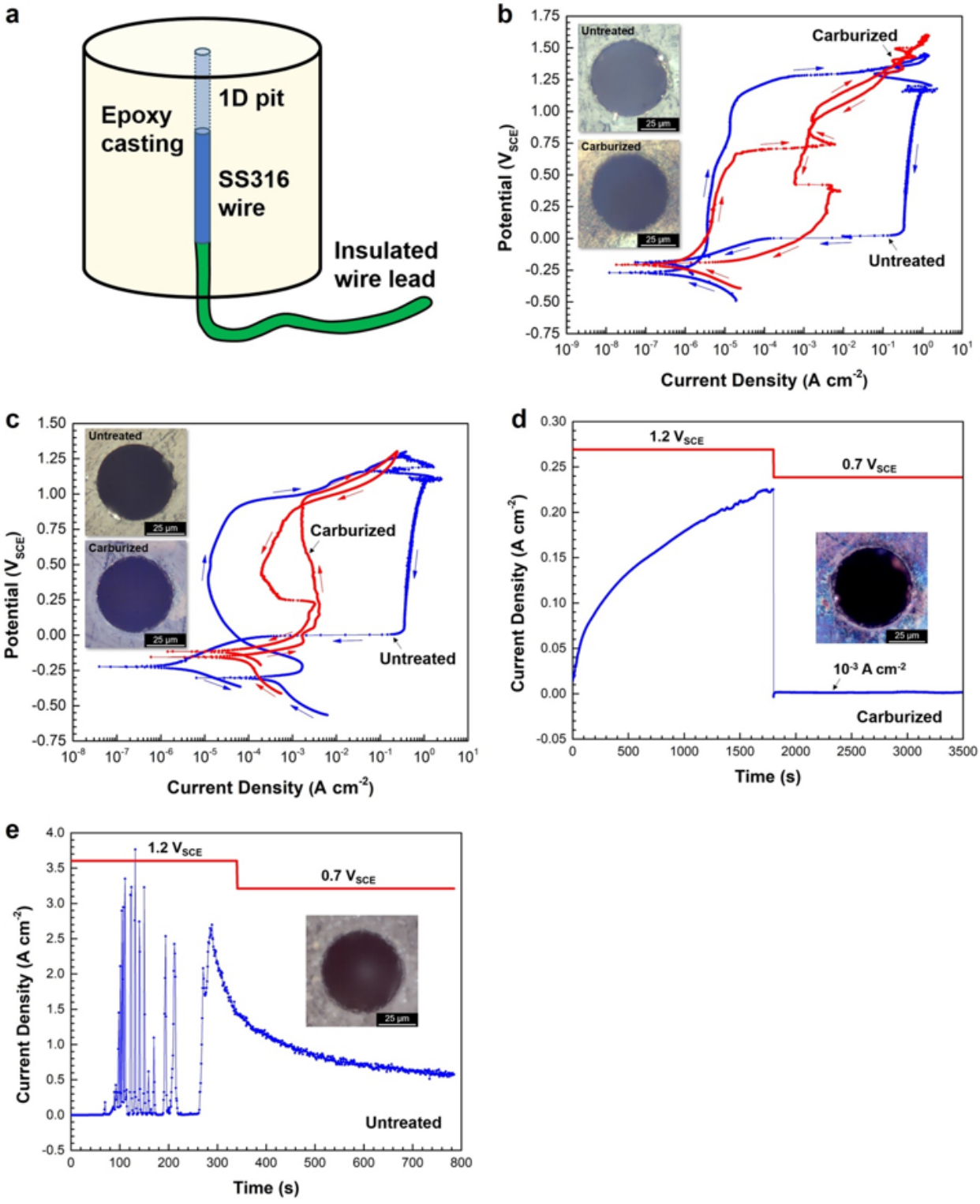

Figure 2

Cyclic potentiodynamic polarization of untreated and carburized SS316 1D artificial pit electrodes in (a) 0.6 M NaCl and (b) 1M HCl solutions at room temperature. Potentiostatic polarization of (c) untreated

and (d) carburized SS316 1D artificial pit electrodes stepping from 1.2 to 0.7 VSCE in 0.6 M NaCl solution at room temperature. The inserted optical images display the morphology of the pit mouth after the test. (e) Schematic of 1D artificial pit electrode.

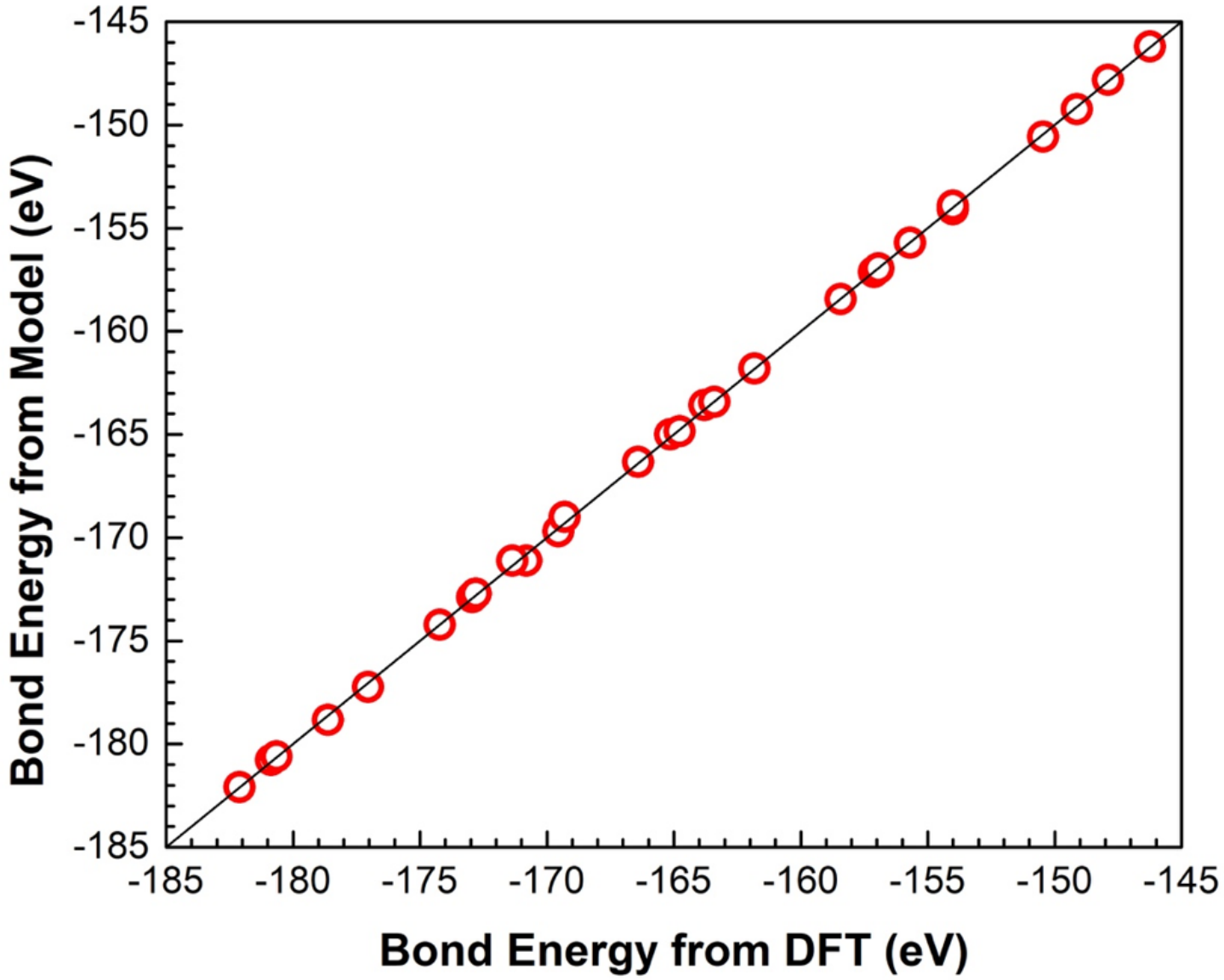

Figure 3

Total bond energies of 32-metal-atom supercell with FCC structure from the fitting (y-axis) vs. the DFT-calculated total bond energies used for the fit (x-axis). Each point represents the total bond energy corresponding to a specific composition in the FeCr:C alloy system. The low energy end (-185 eV) corresponds the composition with high concentration of interstitial carbon, and high energy end (-145 eV) corresponds the composition with low concentration of interstitial carbon. The fit was done with high fidelity (R2 = 0.999).

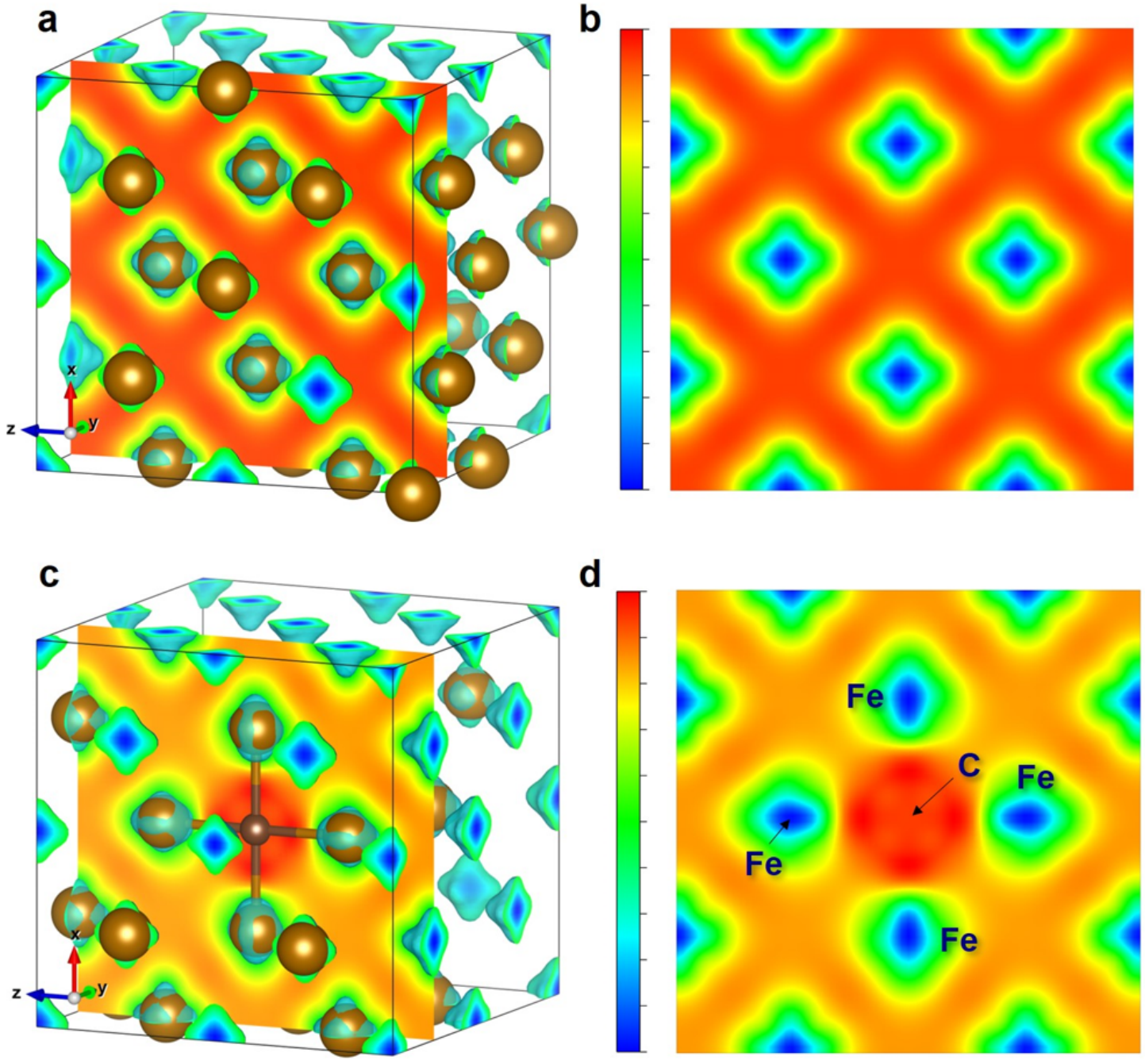

Figure 4

Charge density difference of pure Fe: (a) Constant-charge surfaces with embedded contour plot; (b) Separated contour plot (with a minimum value of -0.0176 bohr/hartree and a maximum value of 0.0016 bohr/hartree). Charge density difference of the Fe with an interstitial carbon occupying the octahedral site formed by Fe atoms: (c) Constant-charge surfaces with embedded contour plot; (d) Separated contour plot (with a minimum value of -0.0117 bohr/hartree and a maximum value of 0.0049 bohr/hartree).

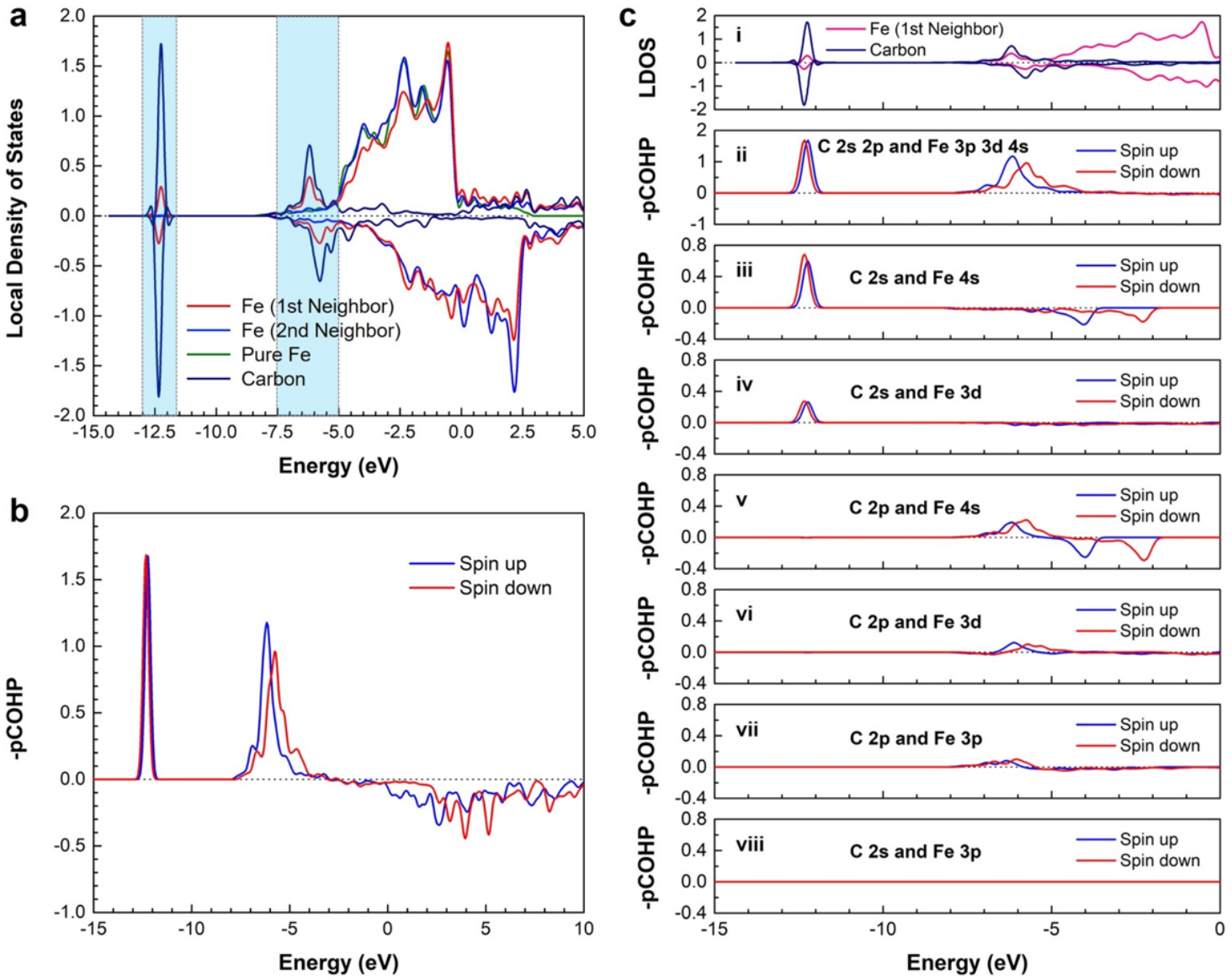

Figure 5

(a) Local density of states for the interstitial carbon (the red curve), the one of the six nearest neighboring Fe atom (the green curve), the second nearest neighboring Fe atom (the blue curve), and a Fe atom in pure iron (the purple curve). (b) Projected crystal orbital Hamilton population (pCOHP) analysis of an interstitial carbon and the first nearest neighbor Fe in a 32-atom Fe supercell obtained by stacking FCC cells with 1 interstitial carbon. (c-i) LDOS of an interstitial carbon and the first nearest neighbor Fe and (c-ii)-(c-viii) pCOHP analysis of different orbital interaction in interstitial carbon and Fe.

Supplementary Files

This is a list of supplementary files associated with this preprint. Click to download.

- LiNMSM.docx